Journal of Vacuum Science Technology B

Assessing stability of metal tellurides as alternative photomask materials for extreme ultraviolet lithography

Running title: Assessing stability of metal tellurides as alternative photomask materials for extreme ultraviolet lithography

Running Authors: Luong et al.

Vu Luong,[a,b] Vicky Philipsen, Karl Opsomer, Jens Rip,
Eric Hendrickx, and Marc Heyns[b]

Imec, Kapeldreef 75, B-3001 Leuven, Belgium

Christophe Detavernier

Cocoon, Solid State Sciences, Universiteit Gent, Zwijnaardsesteenweg 294, B-9000 Gent, Belgium

Christian Laubis, Frank Scholze

Physikalisch-Technische Bundesanstalt (PTB), Abbestraße 2-12, 10587 Berlin, Germany

[a] Electronic mail: vu.luong@imec.be

[b] Also at MTM-SIEM, KU Leuven, Kasteelpark Arenberg 44, B-3001 Leuven, Belgium

Tellurium (Te) is one of the elements with highest extinction coefficient κ at the 13.5 nm extreme-ultraviolet (EUV) wavelength. It is being considered as an alternative absorber material for binary photomask in EUV lithography. The absorber material is required to remain chemically stable during EUV exposure, at elevated temperatures up to 150°C, during mask cleaning, and in the low hydrogen pressure environment that is present in the EUV scanner. However, Te is known to react with oxygen and hydrogen, forming less EUV absorbing TeO_2 and more volatile H_2Te respectively. Since the melting temperature of Te is only 449.5°C at normal pressure, alloying Te with a more stable metal might result

in a high κ material that will remain thermally and chemically stable over a wider range of operating conditions.

In this paper, we report on the stability assessment of metal telluride (M-Te) alloys for EUV absorber material. We combined Te with high κ metals, noble metals, and etchable metals. High κ and noble M-Te materials are both thermally more stable than etchable M-Te, but they cannot be patterned easily for use in an EUV photomask. High κ M-Te exhibit poly-crystal morphology at room temperature compared to quasi-amorphous noble M-Te, though both can crystallize at a higher temperature. Hydrogen stability and cleaning solution stability of M-Te materials are improved considerably compared to Te, but their higher surface reactivity cannot be completely mitigated without the addition of an inert capping layer. Furthermore, etchable M-Te alloys are easily oxidized during deposition, resulting in lower electron density and hence lower κ. Nevertheless, M-Te alloys may be a way to stabilize Te for usage as EUV absorber material.

I. INTRODUCTION

Extreme ultraviolet (EUV) lithography utilizes light at 13.5 nm wavelength to enable patterning of electronic devices, starting at the 7 nm technology node. The EUV photomask is one of the critical components of the scanner, as it contains the pattern to be printed on wafer. State-of-the-art EUV photomasks are comprised of a reflective multilayer (ML) mirror, which contains 40 bilayers of Mo/Si, capped with a 2 nm protective Ru layer, and a 60 nm patterned Ta-based absorber. To reduce mask topography-induced 3D (M3D) effects while maintaining a reasonable contrast between the absorber and the mirror, a thinner absorber would require an alternative absorber material [1]. For binary absorbers, a material with high EUV absorption and low phase deformation is preferred. This translates to a material with a high extinction coefficient κ and refractive coefficient n matching that of vacuum, i.e. close to 1.

As shown in Figure 1, silver (Ag) has the highest EUV absorption, but also a large n mismatch with vacuum. Other high κ materials, such as nickel (Ni) [2-3] and cobalt (Co) [2], have previously been investigated as potential EUV absorber materials. The poly-crystalline morphology of Ni, and Co, increases line-edge-roughness (LER). Elements such as tin (Sn) and indium (In) have low mechanical strength, while antimony (Sb) forms toxic SbH_3 in H_2 atmosphere, the latter being present in EUV scanners [4]. Lastly, there is tellurium (Te), which is among the three highest EUV absorbing elements at 13.5 nm wavelength [5]. Furthermore, the refractive index of Te is relatively close to vacuum.

Next to its desirable optical properties, Te also reacts easily with hydrogen and oxygen, forming H_2Te and TeO_2 respectively [6]. With a melting point at 449.5°C under normal temperature and pressure, Te is thermally less stable than most metallic absorber

candidates. Its chemical reactivity gives Te [7] a patterning advantage as absorber material over many EUV absorbing metals, such as Ni [2], Co [2], Pt [7], Ir [8], Rh [8], etc. These metals are too chemically stable to form volatile by-products during halogen-based plasma etching. Although alternative patterning techniques, such as Atomic Layer Etch (ALE) [9], are emerging, they are currently not ready for high volume manufacturing, and they are mainly used for isotropical etching of layer thicknesses under 10 nm.

By alloying Te with more stable metals, we attempt to engineer an absorber material with high EUV absorption, which is durable under mask usage and cleaning conditions, but still reactive enough to allow patterning. Metal telluride alloys have been investigated for absorbers in the past [10-11], but not as a means to improve durability.

Alternative absorbers promise to reduce M3D effects for beyond 5 nm technology nodes (minimum metal pitch < 24 nm). They are required for insertion with future EUV systems with high numerical aperture of 0.55 [12].

In this paper, we explain our choice of M-Te materials to investigate in Section II, through the combination of Te with either high κ metals, noble metals, or etchable metals. In Section III, we report on the stability assessment of M-Te as EUV absorber material, including thermal stability, stability in hydrogen environment, stability in wet cleaning solutions, and stability against oxidation. Section IV summarizes our results.

II. ENGINEERING METAL TELLURIDES

We investigated three groups of materials: high κ M-Te, noble M-Te, and etchable M-Te. Figure 1 shows the optical constants at 13.5 nm wavelength of the elements

composing the investigated M-Te's, in comparison with the current absorber material TaBN.

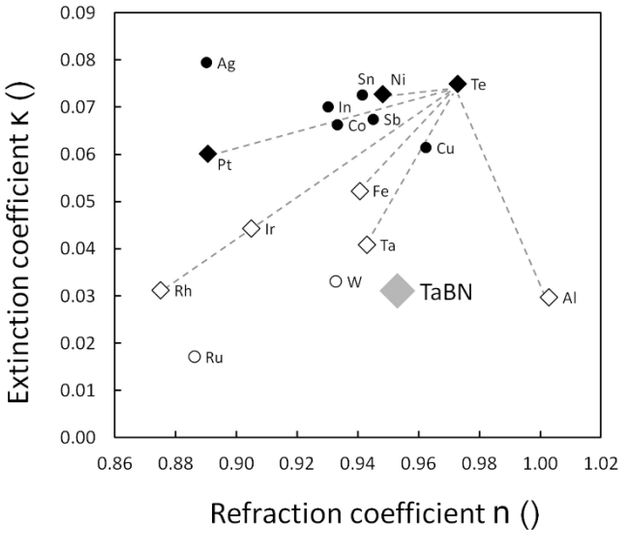

FIG. 1. Optical constants of selected elements at 13.5 nm wavelength. The elements composing the investigated M-Te are represented as diamonds, connected with dashed lines. The nine highest κ elements are colored black. The current absorber material TaBN is represented by a grey diamond [13]. The optical constants are based on Henke's data [5].

High κ M-Te can be alloyed with Ni, Co, or Fe, as these metals are mechanically stable, and have reasonably high extinction coefficients κ. Out of these metals, Ni is the most stable, forming a thin (< 3 nm) passivating surface NiO layer [2], and has the highest κ. Co forms a thicker surface oxide with higher chemical reactivity [2], which suggests easier patterning compared to Ni.

Noble M-Te are alloyed with elements from the platinum-group (elements including Pt, and similar, such as Ru, Rh, Pd, Os, Ir), for their high chemical and thermal stability. Their extinction coefficients κ, while lower than those of NiCoFe transitional metals, can range from relatively high (Pt) to medium (Ir, Rh) to low (Ru). These elements also have a relatively low

refraction coefficient n < 0.92, which results in higher imaging sensitivity to phase deformation, especially when coupled with low EUV absorption.

The etchable M-Te are alloyed with metals that are easily etched with halogen plasma. Ta offers the advantage that it is a commonly used material in the mask industry, while Al offers reduced phase deformation at EUV wavelength due to a refractive coefficient n matched to vacuum. However, we expect that etchable metals will not lead to much higher EUV absorption compared to the current absorber material TaBN.

The M-Te compositions were chosen based on thermodynamic phase diagrams for thermally stable Te-rich alloys, with Te ratio between 40 at% and 80 at%. They are summarized in Table I. $NiTe_2$ and $FeTe_2$ were tested as high κ M-Te materials. $NiTe_2$ was furthermore doped with 10 at% W or Pt to investigate the effect of dopants on crystallinity. The noble M-Te materials include PtTe, IrTe, Ir_3Te_8, Rh_6Te_5, and $Rh_{0.9}Te_2$. The stabilizing effect of a 5 nm metal capping layer was tested for PtTe and $Rh_{0.9}Te_2$, using a Pt- and Rh-cap respectively. The etchable M-Te materials include $TaTe_2$, AlTe, and Al_2Te_3. The goal of engineering M-Te alloys, is to identify a stable, uniform, and quasi-amorphous composition, with high EUV absorption, and selective plasma etchability.

The M-Te samples were deposited with 30 nm nominal film thicknesses by means of physical vapour deposition (PVD). The substrates were 6" Si wafers with 100 nm SiO_2 grown through wet oxidation (500 nm SiO_2 for Ir-Te and Rh-Te). The M-Te materials were deposited using a rotating wafer drum, that sequentially pass through the metal and Te direct current (DC) plasma's at Ar pressures of 5.10^{-3} mbar, resulting in alternating monolayers that instantaneously intermix.

For completeness, we would like to address potential health and safety concerns of Te, an element not unknown in the semiconductor industry [14-16]. The largest risk of Te in

the working environment include inhalational exposure to gaseous H_2Te or TeO_2 dust, and absorption through skin contact [17]. A characteristic sign of tellurium intoxication is the development of a garlic odor of the breath, caused by exhalation of $(CH_3)_2Te$. A possible etch byproduct TeF_6 has been mentioned to be toxic by inhalation in animal tests [17].

III. EXPERIMENTAL RESULTS

In the following sections, we compare the high κ M-Te, noble M-Te, and etchable M-Te for their potential as alternative photomask material. These requirements include thermal stability, stability in a hydrogen environment, stability in wet solutions, and stability against oxidation, as detailed in Luong, et al. (2018) [18].

Table 1 summarizes the experimentally verified density and composition for each sample. Density has been determined from X-ray reflectivity (XRR). Composition is determined with Rutherford Backscattering Spectroscopy (RBS), a technique which is very sensitive to heavy elements, though less so for oxygen. Therefore, other characterization techniques, such as Electron Recoil Detection (ERD) and Energy Dispersive Spectrometry (EDS), were used to determine the composition in oxidized M-Te. The etchable M-Te's, i.e., $TaTe_2$, AlTe, and Al_2Te_3, deviate most from nominal composition due to oxidation, and will be discussed later in Section D on stability against oxidation.

TABLE I. Density and elemental composition of metal tellurides

		Density (g/cm³)	Composition (%)				
			Technique	Metal	Tellurium	Dopant	Oxygen
High κ M-Te	$NiTe_2$	7.17	RBS	35.4	64.6	-	-
	$NiTe_2$-Pt	8.92	RBS	33.4	55.4	11.2	-
	$NiTe_2$-W	8.24	RBS	31.0	55.9	13.1	-
	$FeTe_2$	7.07	EDS	33.0	56.9	-	10.1
Noble M-Te	PtTe	11.54	RBS	50.0	50.0	-	-
	IrTe	11.69	RBS	47.5	52.5	-	-
	Ir_3Te_8	9.69	RBS	27.8	72.2	-	-
	Rh_6Te_5	9.03	RBS	57.7	42.3	-	-
	$Rh_{0.9}Te_2$	8.18	RBS	43.5	56.5	-	-
Etchable M-Te	$TaTe_2$	6.27	EDS	15.0	12.5	-	72.5
	AlTe	3.09	ERD	25.0	18.8	-	56.2
	Al_2Te_3	3.69	ERD	21.7	30.1	-	48.2

A. Thermal stability

The thermal stability of each M-Te material encompasses the assessment of its structural stability, stability of the as-deposited quasi-amorphous morphology against crystallization, and compositional stability, such as volatile formation of Te byproducts at elevated temperatures, as in the case during mask manufacturing or during EUV exposure. With in-situ X-ray diffractometry (IS-XRD) an accelerated lifetime analysis of the M-Te

materials was carried out at temperatures up to 500°C. In practice, EUV photomasks would rarely be exposed to temperatures higher than 150°C due to Mo/Si ML mirror degradation [19]. Cross-section Transmission Electron Microscopy (TEM) was also used to verify the as-deposited morphology. The composition stability was monitored with X-ray fluorescence (XRF).

Figure 2 presents the poly-crystallinity of elemental Te as-deposited, which can result in higher line edge roughness (LER) after patterning. A more preferable quasi-amorphous morphology with nanometer grain sizes can be achieved by alloying Te with other elements. Given enough energy though, the quasi-amorphous can crystallize to a poly-crystalline phase at a higher temperature or over time.

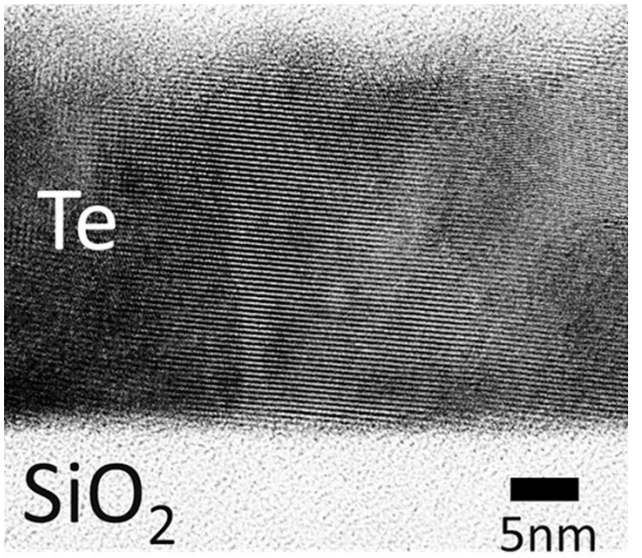

FIG. 2. Cross-section Bright Field Scanning TEM (BF-STEM) image of Te, showing the poly-crystalline morphology.

Therefore, we monitored the M-Te crystallization during anneal from RT up to 500°C with IS-XRD at a ramp rate of 0.2°C/s under He flow. Figure 3 shows the IS-XRD measurements of high κ M-Te, noble M-Te, and etchable M-Te. The color scale uses red

for the highest XRD intensity, white for medium, and blue for low intensity. A high color gradient from blue for the lowest intensity towards red for highest intensity represents a sharp crystalline peak, corresponding to a poly-crystalline morphology. Furthermore, a gradual color gradient signifies a broad peak, corresponding to nano-crystalline or -amorphous morphology. High κ M-Te, such as $NiTe_2$ and $FeTe_2$, are polycrystalline as deposited. However, with the correct dopant, such as $NiTe_2$-W, an amorphous morphology can be achieved as-deposited, and crystallization occurs only above 300°C. For the noble M-Te and etchable M-Te, the absence of peaks at RT means an amorphous structure as-deposited. A poly-crystalline phase starts forming above 200°C, for PtTe, $Rh_{0.9}Te_2$, AlTe, and Al_2Te_3, and above 300°C for Rh_6Te_5.

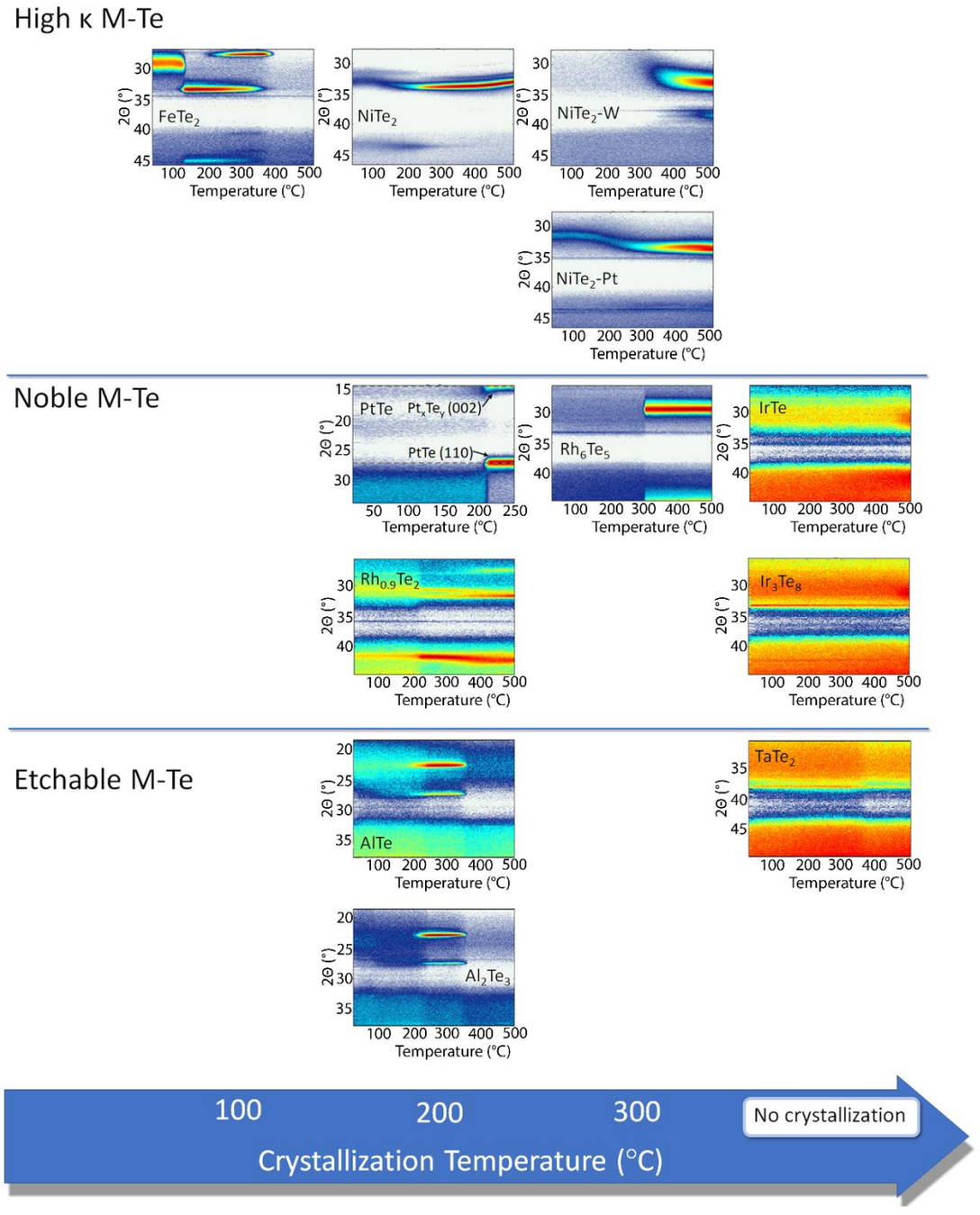

FIG. 3. (Color online) IS-XRD showing changes in crystalline phases as a function of temperature for high κ M-Te: $FeTe_2$, $NiTe_2$, $NiTe_2$-W, $NiTe_2$-Pt; for noble M-Te: PtTe, $Rh_{0.9}Te_2$, Rh_6Te_5, IrTe, Ir_3Te_8; and etchable M-Te: AlTe, Al_2Te_3, $TaTe_2$.

The exceptions are IrTe, Ir_3Te_8, and $TaTe_2$, which stay amorphous from RT up to 500°C. In case crystallization does occur, a high crystallization temperature T_{crys} is preferable, as the material would remain amorphous for a longer time before crystallization would occur at lower constant working temperatures.

In some M-Te's, in which the metal is prone to oxidation (cfr. Section III.D), such as $FeTe_2$, $TaTe_2$, AlTe, and Al_2Te_3, the crystalline peaks can disappear around 350°C.

We investigated the g at 210°C through Kissinger thermal analysis [20], as it is expected to have the highest κ out of all tested noble M-Te [1]. The activation energy E_{ACT} was determined as 2.01 eV, which allows us to estimate the duration for PtTe (110) XRD peak formation at 27° 2θ for a given temperature, as shown in Figure 3-e. The lifetime of quasi-amorphous PtTe is determined as the time where 60% of the material has crystallized and is plotted versus temperature in Figure 4. Based on the kinetic analysis, PtTe has been determined to remain quasi-amorphous for at least 1 year under a constant temperature of 120°C, which is well above the current mask surface temperature during EUV exposure. Furthermore, the photomask backside can be cooled down in-situ to control its thermal load. A detailed report on the kinetic analysis will be covered in a forthcoming paper [21].

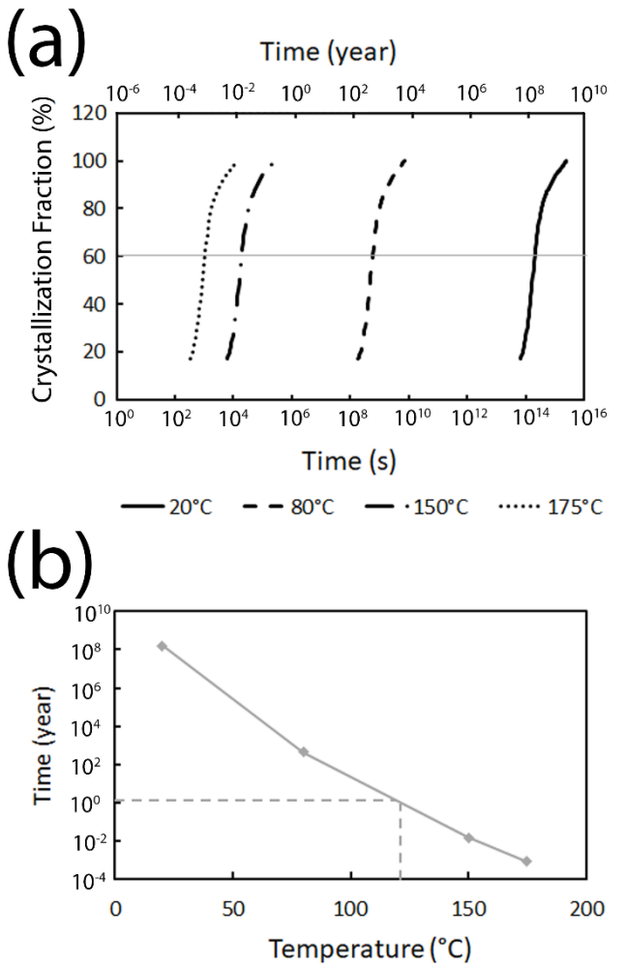

FIG. 4. (a) Simulated PtTe crystallization fraction as function of time. (b) Time to 60% PtTe crystallization fraction as function of temperature.

Apart from crystallization, surface Te can also start melting at 449.5°C at normal pressure, or start forming volatile hydrogen byproducts under vacuum. Therefore, we monitored Te content in the M-Te samples before, and after subsequent thermal loading cycles with XRF. Figure 5 shows the relative Te content of PtTe, $TaTe_2$, AlTe and Al_2Te_3 to as-deposited, after 3 hours at 250°C, and after subsequent annealing up to 500°C. All M-Te's lost more than 90% of their original Te intensity when annealed to 500°C. However, at 250°C the etchable $TaTe_2$ and Al_2Te_3 already exhibit more than 30% Te

intensity loss after 3 hours. For these materials, this indicates either that the surface is Te-rich, or that Te diffusion from bulk to the surface is easier. Additionally, we verified pronounced oxidized Al, Ta, and Te peaks with Angle Resolved X-ray Photospectroscopy (AR-XPS). Therefore, we believe there is preferential binding of Ta and Al to O, resulting in weaker Ta-Te and Al-Te bonds, and hence higher Te reactivity in these M-Te alloys. On the other hand, $NiTe_2$-W, PtTe, and AlTe exhibit limited Te loss in this condition. For $NiTe_2$-W and PtTe, a chemically stable surface, such as Pt or NiO, could reduce surface reactivity, while W-doping could reduce Te diffusion from bulk to surface. AlTe lost less Te compared to Al_2Te_3 due to smaller Te content.

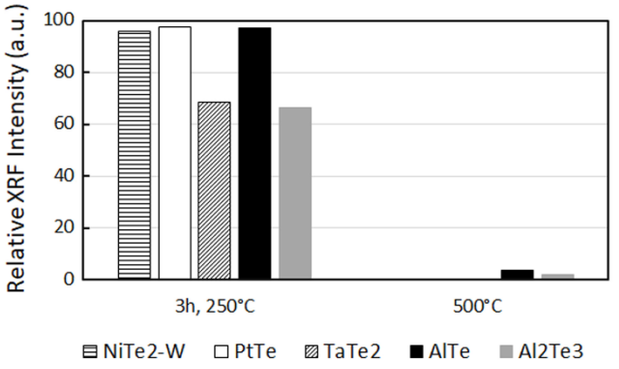

FIG. 5. X-Ray Fluorescence (XRF) intensity of Te in $NiTe_2$-W, PtTe, $TaTe_2$, AlTe, and Al_2Te_3 after 3 hours at 250°C, and after subsequent annealing to 500°C relative to the as-deposited reference sample.

Based on these experiments, we can conclude that noble M-Te, and in particular, the Ir-Te alloys are the most thermally stable, as its amorphous morphology remains at higher temperature. High κ M-Te crystallizes at a certain temperature, but using specific dopants can postpone crystallization to higher temperatures, such as in the case of $NiTe_2$-W. Etchable M-Te lose Te more easily under thermal load, though in the case of $TaTe_2$ the morphology will not change.

B. Hydrogen stability

Hydrogen stability assessment was performed to mimic scanner condition. In the first experiment, the samples were exposed at 15 Pa for 24 hours in an H_2/H* environment, created by a hot tungsten filament [22]. The resulting elemental composition change was compared to a reference sample using RBS and ERD, which is expressed in Thin Film Units (1 TFU = 10^{15} atoms/cm^2). A second experiment performed at PTB, exposed the samples at a lower H_2 pressure of maximum 3 Pa, in combination with high power EUV light up to 250W corresponding to a power density of 5W/cm^2 [23]. PtTe samples were exposed for 30 minutes, after which the surface and bulk compositions were determined with AR-XPS.

The results of the first hydrogen stability assessment experiment are shown in Figure 6. A relative TFU larger than 100% might indicate a composition variation for a specific element between the reference and the tested sample.

The reference Te has reacted away after 24 hours in H_2/H*. For the M-Te alloys, three groups can be distinguished: materials in which after reaction with H_2/H* (1) neither metal nor Te is reduced more than 20% ($NiTe_2$-Pt, $FeTe_2$, PtTe, PtTe/Pt, $Rh_{0.9}Te_2$/Rh, and $TaTe_2$); (2) only Te is reduced more than 20% ($NiTe_2$ and Al_2Te_3); and (3) both metal and Te is reduced more than 20% ($NiTe_2$-W, IrTe, Ir_3Te_8, and Rh_6Te_5). For group (3) materials an irregularly blotched surface can be observed, which indicates a heterogeneous surface reaction. However, Figure 6-b shows that by using a thin metallic capping layer, such as 5 nm Rh-capped $Rh_{0.9}Te_2$ ($Rh_{0.9}Te_2$/Rh) and 5 nm Pt-capped PtTe (PtTe/Pt), the surface Te reaction can be inhibited. Dopants could also impact surface reaction. 10 at% Pt reduces surface Te reaction in $NiTe_2$. On the other hand, 10 at% W deteriorates the hydrogen

stability of $NiTe_2$. Possibly this is caused by W replacing some of the surface Ni, hereby inhibiting the formation of stable NiO. Even for group (1) M-Te, where the relative TFU is close to 100%, some visible surface reaction can still be observed, such as speckle formation, pitting ($NiTe_2$-Pt), or discoloration ($TaTe_2$).

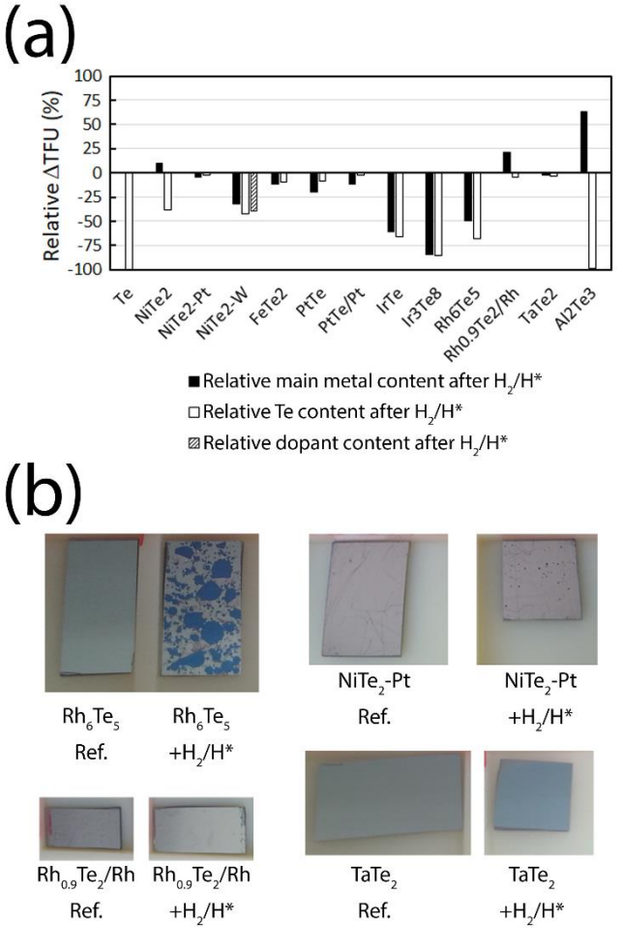

FIG. 6. (Color online) (a) M-Te samples are measured with RBS before and after 24 hours in H_2/H* environment at 15 Pa. The Thin Film Unit (1 TFU = 10^{15} atoms/cm^2) difference relative to the condition before the H_2/H* test is compared between different M-Te. (b) Images of Rh_6Te_5, $Rh_{0.9}Te_2$/Rh, $NiTe_2$-Pt and $TaTe_2$: reference sample on the left versus the sample after H_2/H* test on the right. The blue substrate is SiO_2.

To mimic the environment in the reticle chamber, no H* will be actively formed, and the H_2 pressure should be lower than 15 Pa, this in combination with simultaneous EUV exposure.

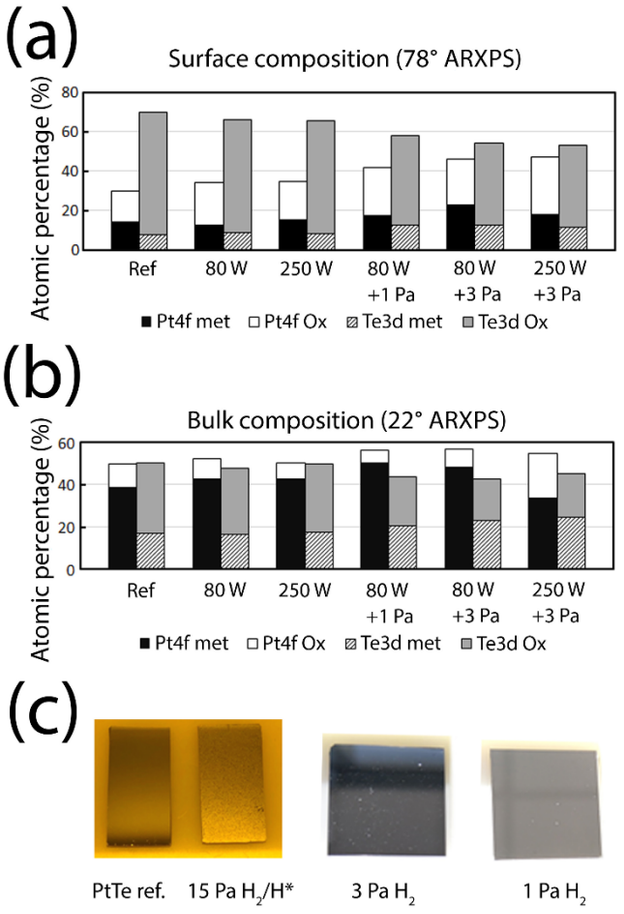

FIG. 7. (Color online) PtTe after different combinations of EUV power and H_2 pressure. (a) Surface, and (b) bulk composition were determined with AR-XPS. Pt 4f and Te 3d metallic and oxide peaks are used for quantification. AR-XPS can probe as deep as 10 nm from the sample surface. (c) Images of PtTe: reference, after 24 hours at 15 Pa H_2/H*, after 30 minutes at 250W EUV 3 Pa H_2, and after 30 minutes at 80W EUV 1 Pa H_2. 250 W and 80 W correspond to a power density of 5 and 1.6 W/cm^2 respectively.

The AR-XPS measurements in Figure 7-a show that the reference PtTe surface is Te-rich, which is predominantly oxidized. Under EUV exposure without H_2 flow, the composition becomes slightly less Te-rich, while no significant difference is observed in the metal:oxide ratio. However, the largest impact is caused by the presence of H_2. Especially the surface composition changes from Te-rich towards a ratio closer to 1:1 Pt:Te, due to reaction of unbound surface Te with H_2. The bulk composition also changes slowly from a 1:1 Pt:Te ratio towards a slightly Pt-rich composition. Furthermore, the amount of metallic Pt and Te increases with higher H_2 pressure, due to reduction of oxidized Pt and Te by H_2. The PtTe bulk after 250 W EUV exposure and 3 Pa H_2 seems to be more oxidized, which could be attributed to the increased surface roughness, allowing more material to be reoxidized. An increase in surface roughness is also observed with higher H_2 pressure, as shown in Figure 7-c. These results are expected due to high reactivity of Te with H_2, but they also show that alloying Te with a suitable metal can limit Te reaction towards the surface. While such pronounced surface roughness could complicate patterning absorbers with these materials, there are options to stabilize their chemical reactivity, and to further optimize processing for low roughness.

C. Stability in solutions

To test the material stability during photomask cleaning process, we have determined the dissolution rate in cleaning solutions with Inductively Coupled Plasma Mass Spectrometry (ICP-MS) on an Agilent 7500cs instrument. Two baseline solutions in photomask cleaning processes were tested: deionized water (DIW) at pH 5.7 and 1% ammonium hydroxide solution (NH_4OH) at pH 11.4 [24]. We did not test acidic cleaning solutions as they generally have higher reactivity with metals, and they cause peeling of the protective Ru-capping layer on the Mo/Si

ML mirror [24]. The sample surface was submerged for 27 hours, with solutions being collected for analysis and new solution being added at 1, 2, 3, and 27 hours. The dissolved Te concentration in DIW and in NH_4OH was monitored over time, using ^{125}Te signal for quantification. A 70 nm TaBN mask sample was also tested as reference.

Elemental Te exhibited limited thickness loss in DIW, and dissolved almost completely in NH_4OH cleaning solutions within 90 minutes. According to Pourbaix [25], Te is expected to react in either very alkaline solutions to Te^{2-} or Te_2^{2-} , and in aerated water to TeO_2. A layer of TeO_2 is sparingly soluble at pH 4 to 7, with a calculated minimum solubility of 8.1 ng Te /ml at pH 5.45 based on historical results [25]. However, experimental values for Te solubility have been reported three magnitudes higher around 5.3×10^3 ng Te /ml at pH 7 [25]. Te would remain inert in aqueous solutions free from oxidizing agents.

We tested noble M-Te materials, as they showed no clear chemical reaction after one day submersion, such as discoloration, or significant thickness loss as determined with XRR. The dissolution behavior of IrTe in DIW is shown as example in Figure 8-a. A sample is submerged subsequently with fresh solution, once every hour for the first 3 hours, and then one final time for 24 hours. After submersion the solutions are collected and analyzed with ICP-MS.

A non-linear dissolution rate is observed, where most material is dissolved within the first hour, and where the dissolution slows down over time. When the solvent is renewed between each data point, the additional mass dissolved is only marginal after subsequent renewal, regardless of submersion time. This implies that the dissolution is limited by the available dissolvable material on the surface. Also, Te dissolves more quickly from the alloy than the metallic element. The slope of dissolved mass over the first hour, normalized to the solvent volume, is shown in Figure 8-b for noble M-Te materials.

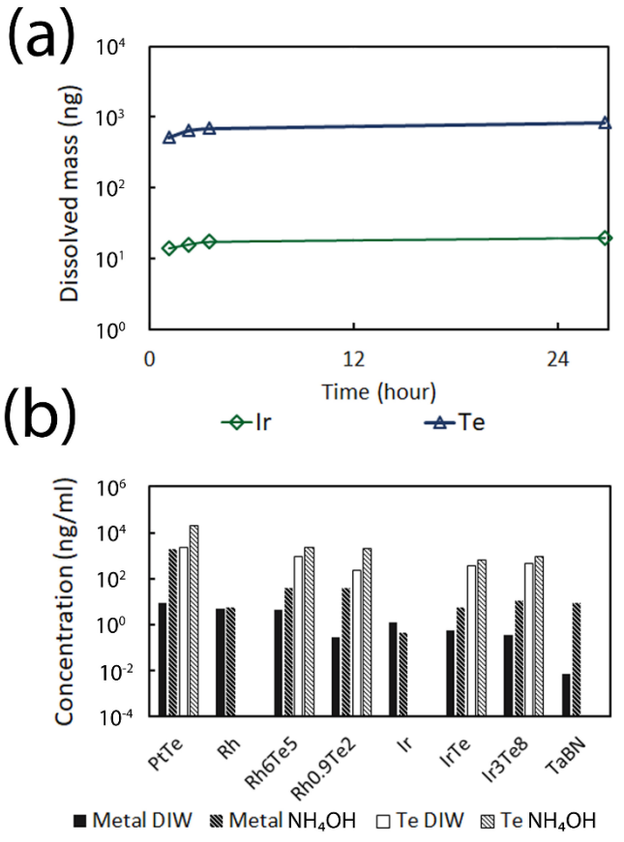

FIG. 8. (Color online) (a) Non-linear dissolution behavior of IrTe in DIW over time, with Ir and Te depicted by diamond and triangle markers respectively; (b) Comparison of the concentration in ng per ml solvent after 1 hour submersion between noble M-Te and TaBN.

The TaBN mask sample dissolved very little due to the low Ta solubility in aqueous solutions, and due to the passivating TaBO top layer. As for the M-Te, more material dissolves in NH_4OH, compared to DIW; and Te is more soluble than metals. Elementary noble metals have the lowest solubility, but it increases when alloyed with the more reactive Te, especially in NH_4OH. Pt-based M-Te is more soluble than Rh_xTe_y, which in turn is more soluble than Ir_xTe_y. Surprisingly, increasing the Te-to-metal ratio increases neither metal nor Te solubility significantly with the tested M-Te compositions. The

presence of Te on the surface likely compromises the formation of a passivating native metal oxide surface layer. Indeed, a 5 nm metal capping layer reduces both metal and Te solubility in DIW, and even more in NH_4OH, as shown in Figure 9. The effect of a capping layer has a larger effect on PtTe, likely due to its higher solubility than $Rh_{0.9}Te_2$.

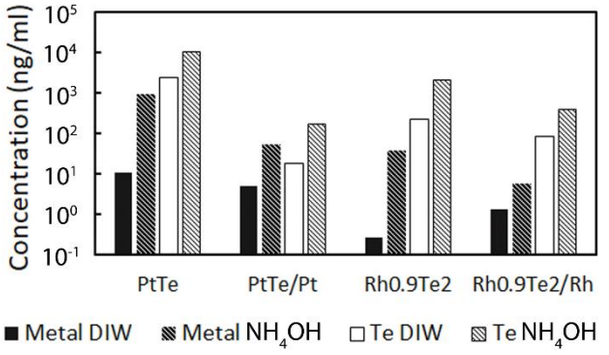

FIG. 9. Comparison of the concentration in ng per ml after 1 hour submersion between uncapped M-Te and M-Te capped with a 5 nm thick metallic layer.

The Te solubility values from this experiment are closer to the experimental values reported Erdmann, et al. (2017) [26], than to the calculated Te solubility. This is possibly due to diffusion of oxidizing agents from ambient into the solutions. To simulate real mask cleaning processes, while considering non-linear solubility, the dissolution time can be lowered to 30 minutes and shorter, but the impact on repeatability will need to be assessed.

D. Oxidation stability

Stability against oxidation is important for alternative absorber candidates, as the extinction coefficient κ is directly proportional to the electron density of the material [1]. Oxidation usually decreases the material density, as well as reducing the high κ element ratio, resulting in less EUV absorption. A small degree of oxidation can be allowed if the absorber material forms a self-limiting native oxide layer, such as is the case with Ni [2].

Elemental Te however oxidizes easily in ambient air, as shown on the High Annular Angular Dark Field Scanning Transmission Microscopy (HAADF-STEM) image shown in Figure 10-a, where contrast is proportional to the square atomic charge $<Z^2>$. The area with darker contrast in the Te layer indicate the presence of lighter elements, such as oxygen. Figure 10-a shows that the Te layer is mostly oxidized, with few metallic Te grains. On the other hand, PtTe is more resistant to oxidation than Te. On Figure 10-b there is less contrast in the PtTe layer and the surface is also smoother. The brighter grains are richer in Pt than the PtTe layer.

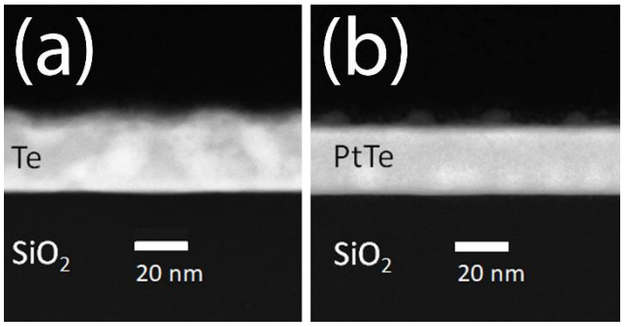

FIG. 10. Cross-section HAADF-STEM images of (a) Te and (b) PtTe. Darker area in the indicate the presence of lighter elements, such as O in the Te layer, or Te and O in the PtTe layer.

According to Table I, all tested noble M-Te, and most high κ M-Te are resistant to oxidation, with Te oxidation only occurring in the first few monolayers on the surface. $FeTe_2$ and the etchable M-Te however, are more prone to oxidation, with the latter easily oxidizing throughout the full layer when left in ambient air. In Figure 11, the Ta4f and Te3d peaks are measured with AR-XPS for $TaTe_2$. No metallic Ta peaks were observed. The metallic Te peaks are smaller than the oxidized Te peaks, and more metallic Te can be found towards the bulk. Although XPS is only sensitive to the top 10 nm, XRR corroborates

a low $TaTe_2$ density similar to the theoretical density of Ta_2O_5 and Te/TeO_2, as shown in Figure 11-c. We can conclude that a Ta:Te ratio of 1:2 is very sensitive to oxidation.

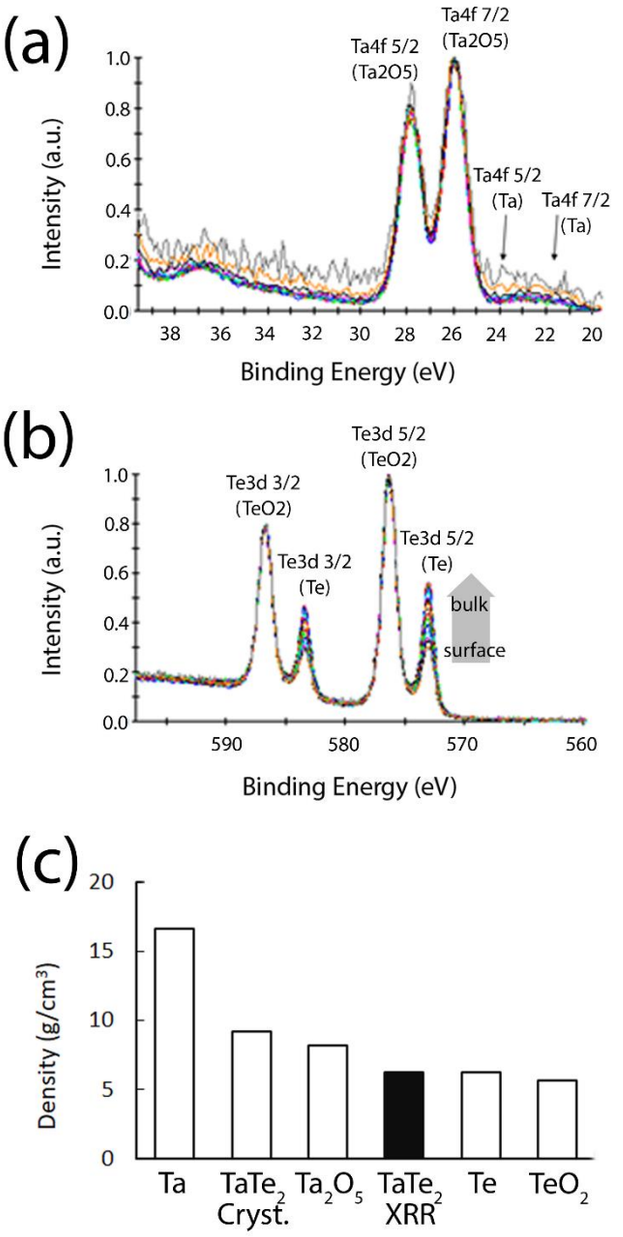

FIG. 11. (Color online) AR-XPS of (a) Ta, and (b) Te peaks in $TaTe_2$, showing predominantly oxidized peaks. (c) Experimentally determined density of $TaTe_2$ (black

bar) , compared to theoretical density of crystalline Ta, $TaTe_2$, Ta_2O_5, Te, and TeO_2 (white bars).

M-Te can also be prone to oxidation over time, which will need to be monitored. Depending on the ease of oxidation, a top surface capping layer might be sufficient as passivation. Ideally the absorber sidewall should also be capped, but this would complicate mask processing, and its effect on oxidation is smaller compared to a top surface capping layer as long as the sidewall area is smaller compared to top surface area.

IV. SUMMARY

The optical properties of Te make it promising as an alternative EUV absorber for binary photomasks, as a high extinction coefficient κ allows the implementation of thinner absorbers, resulting in M3D reduction. We have shown that by alloying Te with certain metals, its thermal stability, stability in hydrogen environment, oxidation stability, and stability in cleaning solutions can be improved significantly compared to elemental Te. The crystalline structure of Te can be avoided as-deposited and postponed over time by pushing towards higher crystallization temperature. Nevertheless, the improved alloys do not yet show the full stability and process capability that is needed. Te will be lost from M-Te as its temperature approaches the normal melting temperature of elemental Te at 449.5 °C, although in mask making processes temperatures are usually not higher than 150 °C. The Te stability against hydrogen reaction, oxidation and in cleaning solutions is limited, especially near surfaces where Te reactivity is higher than in bulk. The solubility of M-Te materials in tested aqueous solutions is non-linear, and Te dissolves more quickly in basic solutions. Most etchable M-Te are also prone to oxidation, resulting in lower density, lower

κ, and lower EUV absorption compared to noble and high κ M-Te materials. Provided the Te reactivity is limited towards a few monolayers, a top surface capping layer should be considered to improve M-Te stability. Currently, there seems to be a trade-off between the two most critical properties: optical constants and plasma etchability. M-Te alloys with the highest κ contain metals that cannot easily form volatile by-products, and vice versa. Issues with morphology, roughness, and chemical stability, could be mitigatable through optimizing processing parameters, dopants, and capping layer.

TABLE II. Tested M-Te are ranked to absorber requirements. Best result per requirement is stated in bold. Best material per group is between brackets.

Absorber requirements	Elemental Te	High κ M-Te	Noble M-Te	Etchable M-Te
Optical constants (high κ)	**Highest**	**Highest** ($NiTe_2$-Pt)	High (Pt-Te)	Low ($TaTe_2$)
Morphology/ Thermal stability/	Poly-cryst. as-dep; Melting temp ~449.5°C	Q.-amorph. as-dep only; **Te-loss ~500°C** ($NiTe_2$-W)	**Q.-amorph. ~500°C; Te-loss ~500°C** (Ir-Te)	**Q.-amorph. ~500°C**; Te-loss <500°C ($TaTe_2$)
Hydrogen stability	Low	**High** ($NiTe_2$-Pt)	Limited (Pt-Te)	**High** ($TaTe_2$)
Cleaning stability	Reacts with DIW and NH_4OH	Reacts with NH_4OH (all)	**Highest** (Ir-Te)	High ($TaTe_2$)
Oxidation stability	Low	High ($NiTe_2$-Pt)	**Highest** (Pt-Te & Ir-Te)	Limited ($TaTe_2$)
Plasma etchability	No optimized Te etch, but halogen plasma etchable	No developed Ni etch	No developed Pt/Ir etch	**Developed Ta etch**

Table II summarizes and ranks the M-Te classes according to the required properties for EUV absorbers. High κ M-Te's have the potential for highest extinction coefficient, but would require a different alkaline cleaning solution than NH_4OH. Noble M-Te's rank best or second best for most properties, but have higher H_2 reactivity. While only $TaTe_2$ is sufficiently stable of those tested, with relatively lower scores for κ, thermal, and oxidation stability compared to other tested M-Te materials, it is also the only candidate that can be etched with existing halogen plasma technology. Therefore, the development of Ta-Te-X alloys in the short term could yield an alternative absorber material with higher κ and n better matched to vacuum compared TaBN, while simultaneously a new plasma etch technology can be developed for Ni, Pt, or Ir, to resolve this bottleneck. Cleaning solutions need to be developed for alloys, which can address solubility difference between elements, and uncapped sidewalls. Emerging etch technologies need to be able to provide solutions for the formation of volatile by-products, remaining selective to the Ru capping layer, and minimizing the litho-etch bias.

ACKNOWLEDGMENTS

This project has received funding from the Electronic Component Systems for European Leadership Undertaking under grant agreement number 662338. This Joint Undertaking receives support from the European Union's Horizon 2020 research and innovation program and from the Netherlands, France, Belgium, Germany, Czech Republic, Austria, Hungary, and Israel. The authors acknowledge Furuya Metal Co., Ltd. for providing the Ir-Te and Rh-Te alloys. We are grateful to C. Adelmann and S. Mertens

(IMEC) for their thin film expertise. For metrology support, we thank J. Meersschaut, T. Conard, H. Bender, I. Pollentier, N. Vandenbroeck, and A. Pacco (IMEC). We especially appreciate the support of K. Ronse, and S. Van Elshocht (IMEC). We would like to thank O. Wood for his advice and support.

REFERENCES

[1] V. Luong, V. Philipsen, K. Opsomer, E. Hendrickx, M. Heyns, V. Soltwisch, C. Laubis and F. Scholze, [to-be-published]

[2] V. Philipsen, V. Luong, L. Souriau, A. Erdmann, D. Xu, P. Evanschitzky, R. W. E. van de Kruijs, A. Edrisi, F. Scholze, C. Laubis, M. Irmscher, S. Naasz, C. Reuter and E. Hendrickx, J. Micro-Nanolith. Mem. **16**, no. 4, 041002 (2017).

[3] A. Rastegar, M. House, R. Tian, T. Laursen, A. Antohe and P. Kearney, Proc. SPIE **9048**, 90480L (2014).

[4] S. Bajt, *Optics contamination in EUV Lithography*, edited by V. Bakshi (SPIE and John Wiley & Sons, USA, 2009), pp. 229-230.

[5] B. Henke, E. Gullikson and J. Davis, At. Data Nucl. Data Tables **54**, no. 2, pp. 181-342, (1993).

[6] G. Schweitzer and L. Pesterfield, *The aqueous chemistry of the elements* (Oxford University Press Inc., Oxford, 2010).

[7] V. Philipsen, V. Luong, K. Opsomer, C. Detavernier, E. Hendrickx, A. Erdmann, P. Evanschitzky, R. W. E. van de Kruijs, Z. Heidarnia-Fathabad, F. Scholze and C. Laubis, Proc. SPIE **10810,** 108100C (2018).

[8] V. Philipsen, V. Luong, K. Opsomer, L. Souriau, J. Rip, C. Detavernier, A. Erdmann, P. Evanschitzky, C. Laubis, P. Hönicke, V. Soltwisch and E. Hendrickx, Proc. SPIE **11178**, 111780F (2019).

[9] K. J. Kanarik, S. Tan, W. Yang, T. Kim, T. Lill, A. Kabansky, E. A. Hudson, T. Ohba, K. Nojiri, J. Yu, R. Wise, I. L. Berry, Y. Pan, J. Marks and R. A. Gottscho, J. Vac. Sci. Technol. A **35**, 05C302 (2017).

[10] H. Kang, S. Park, J. Lim, P. Peranantham and C. Hwangbo, P. Soc. Photo-Opt. Ins., FC1 (2013).

[11] S. Park, J. Lim, P. Peranantham, H. Kang, C. Hwangbo, S. Lee and S. Kim, Appl. Opt. **53**, no. 4, pp. A42-A47 (2014).

[12] J. Van Schoot, E. Van Setten, K. Troost, F. Bornebroek, R. Van Ballegoij, S. Lok, J. Stoeldraijer, J. Finders, H. Meiling, P. Graeupner, P. Kuerz, W. Kaiser, E. Loopstra, B. Kneer and S. Migura, Proc. SPIE **10809**, 108090Z (2018).

[13] F. Scholze, C. Laubis, K. Luong and V. Philipsen, Proc. SPIE **10446**, 1044609 (2017).

[14] K. Zweibel, Science **328**, no. 5979, pp. 699-701 (2010).

[15] S. Lin, W. Li, Z. Chen, J. Shen, B. Ge and Y. Pei, Nat. Commun. **7**, no. 10287 (2016).

[16] G. Atwood, Science **321**, no. 5886, pp. 210-211 (2008).

[17] L. Gerhardsson, *Tellurium in Handbook on the Toxicology of Metals (Fourth Edition)* Vol. 2, edited by G.F. Nordberg, B.A. Fowler, M. Nordberg (Academic Press, 2015).

[18] V. Luong, V. Philipsen, E. Hendrickx, K. Opsomer, C. Detavernier, C. Laubis, F. Scholze and M. Heyns, Appl. Sci. **8**, no. 4, p. 521 (2018).

[19] P. B. Mirkarimi and C. Montcalm, Proc. SPIE **3331** (1998).

[20] A. Leenaers, S. van den Berghe and C. Detavernier, Solid State Sci. **14**, no. 8, pp. 1133-1140 (2012).

[21] K. Opsomer [to-be-published].

[22] I. Pollentier, J. Vanpaemel, J. U. Lee, C. Adelmann, H. Zahedmanesh, C. Huyghebaert and E. E. Gallagher, Proc. SPIE **9776**, 977620 (2016).

[23] R. Klein, F. Scholze, R. Thornagel, J. Tummler, M. Wedowski, R. Jansen, B. Mertens, A. van de Runstraat and G. Ulm, SPIE **4782**, 2002.

[24] D. Dattilo, U. Dietze and J. Hsu, Proc. SPIE **9635**, 96351B (2015).

[25] M. Pourbaix, *Tellurium in Atlas of Electrochemical Equilibria in Aqueous Solutions* (National Association of Corrosion Engineers , Houston, TX, USA, 1974).

[26] A. Erdmann, D. Xu, P. Evanschitzky, V. Philipsen, V. Luong and E. Hendrickx, Adv. Opt. Technol**. 3-4**, no. 6, pp. 187-201 (2017).

LIST OF TABLES

TABLE I. Density and elemental composition of metal tellurides

		Density (g/cm³)	Composition (%)				
			Technique	Metal	Tellurium	Dopant	Oxygen
High κ M-Te	$NiTe_2$	7.17	RBS	35.4	64.6	-	-
	$NiTe_2$-Pt	8.92	RBS	33.4	55.4	11.2	-
	$NiTe_2$-W	8.24	RBS	31.0	55.9	13.1	-
	$FeTe_2$	7.07	EDS	33.0	56.9	-	10.1
Noble M-Te	PtTe	11.54	RBS	50.0	50.0	-	-
	IrTe	11.69	RBS	47.5	52.5	-	-
	Ir_3Te_8	9.69	RBS	27.8	72.2	-	-
	Rh_6Te_5	9.03	RBS	57.7	42.3	-	-
	$Rh_{0.9}Te_2$	8.18	RBS	43.5	56.5	-	-
Etchable M-Te	$TaTe_2$	6.27	EDS	15.0	12.5	-	72.5
	AlTe	3.09	ERD	25.0	18.8	-	56.2
	Al_2Te_3	3.69	ERD	21.7	30.1	-	48.2

TABLE II. Tested M-Te are ranked to absorber requirements. Best result per requirement is stated in bold. Best material per group is between brackets.

Absorber requirements	Elemental Te	High κ M-Te	Noble M-Te	Etchable M-Te
Optical constants (high κ)	**Highest**	**Highest** ($NiTe_2$-Pt)	High (Pt-Te)	Low ($TaTe_2$)
Morphology/ Thermal stability/	Poly-cryst. as-dep; Melting temp ~449.5°C	Q.-amorph. as-dep only; **Te-loss ~500°C** ($NiTe_2$-W)	**Q.-amorph. ~500°C; Te-loss ~500°C** (Ir-Te)	**Q.-amorph. ~500°C**; Te-loss <500°C ($TaTe_2$)
Hydrogen stability	Low	**High** ($NiTe_2$-Pt)	Limited (Pt-Te)	**High** ($TaTe_2$)
Cleaning stability	Reacts with DIW and NH_4OH	Reacts with NH_4OH (all)	**Highest** (Ir-Te)	High ($TaTe_2$)
Oxidation stability	Low	High ($NiTe_2$-Pt)	**Highest** (Pt-Te & Ir-Te)	Limited ($TaTe_2$)
Plasma etchability	No optimized Te etch, but halogen plasma etchable	No developed Ni etch	No developed Pt/Ir etch	**Developed Ta etch**

LIST OF FIGURES

from the sample surface. (c) Images of PtTe: reference, after 24 hours at 15 Pa H_2/H*, after 30 minutes at 250W EUV 3 Pa H_2, and after 30 minutes at 80W EUV 1 Pa H_2. 250 W and 80 W correspond to a power density of 5 and 1.6 W/cm^2 respectively.

FIG. 8. (Color online) (a) Non-linear dissolution behavior of IrTe in DIW over time, with Ir and Te depicted by diamond and triangle markers respectively; (b) Comparison of the concentration in ng per ml solvent after 1 hour submersion between noble M-Te and TaBN.

FIG. 9. Comparison of the concentration in ng per ml solvent after 1 hour submersion between uncapped M-Te and M-Te capped with a 5 nm thick metallic layer.

FIG. 10. Cross-section HAADF-STEM images of Te. Darker area in the indicate the presence of lighter elements, such as O in the Te layer, or Te and O in the PtTe layer.

FIG. 11. (Color online) AR-XPS of (a) Ta, and (b) Te peaks in $TaTe_2$, showing predominantly oxidized peaks. (c) Experimentally determined density of $TaTe_2$ (black bar), compared to theoretical density of crystalline Ta, $TaTe_2$, Ta_2O_5, Te, and TeO_2 (white bars).

Journal of Vacuum Science Technology B

PLEASE CITE THIS ARTICLE AS DOI: 10.1116/1.5125662

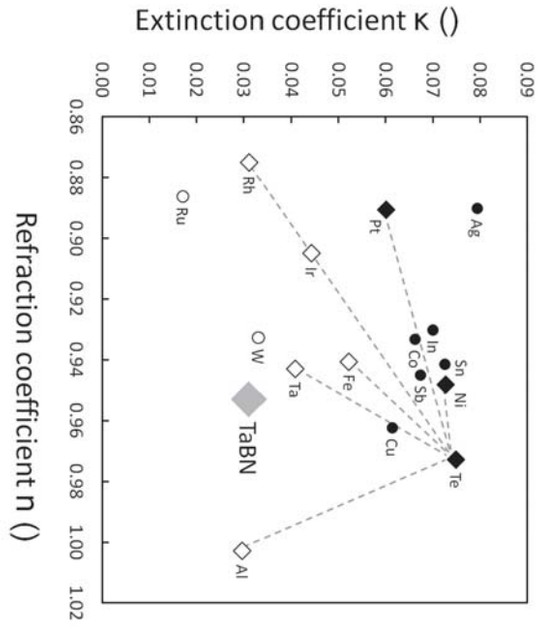

Journal of Vacuum Science Technology B

PLEASE CITE THIS ARTICLE AS DOI: 10.1116/1.5125662

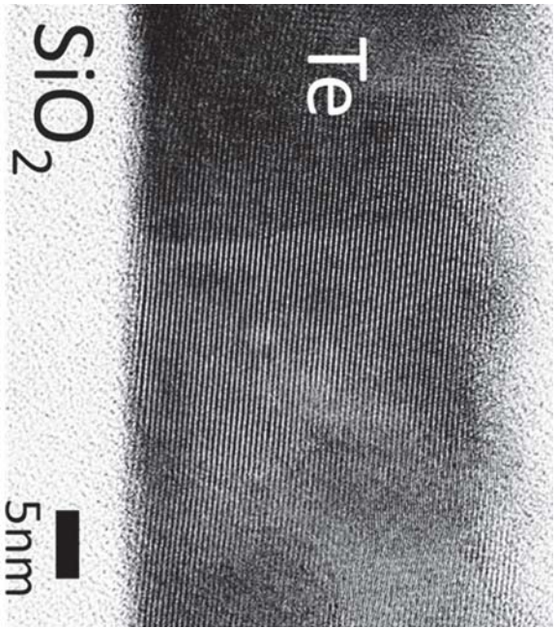

Journal of Vacuum Science Technology B

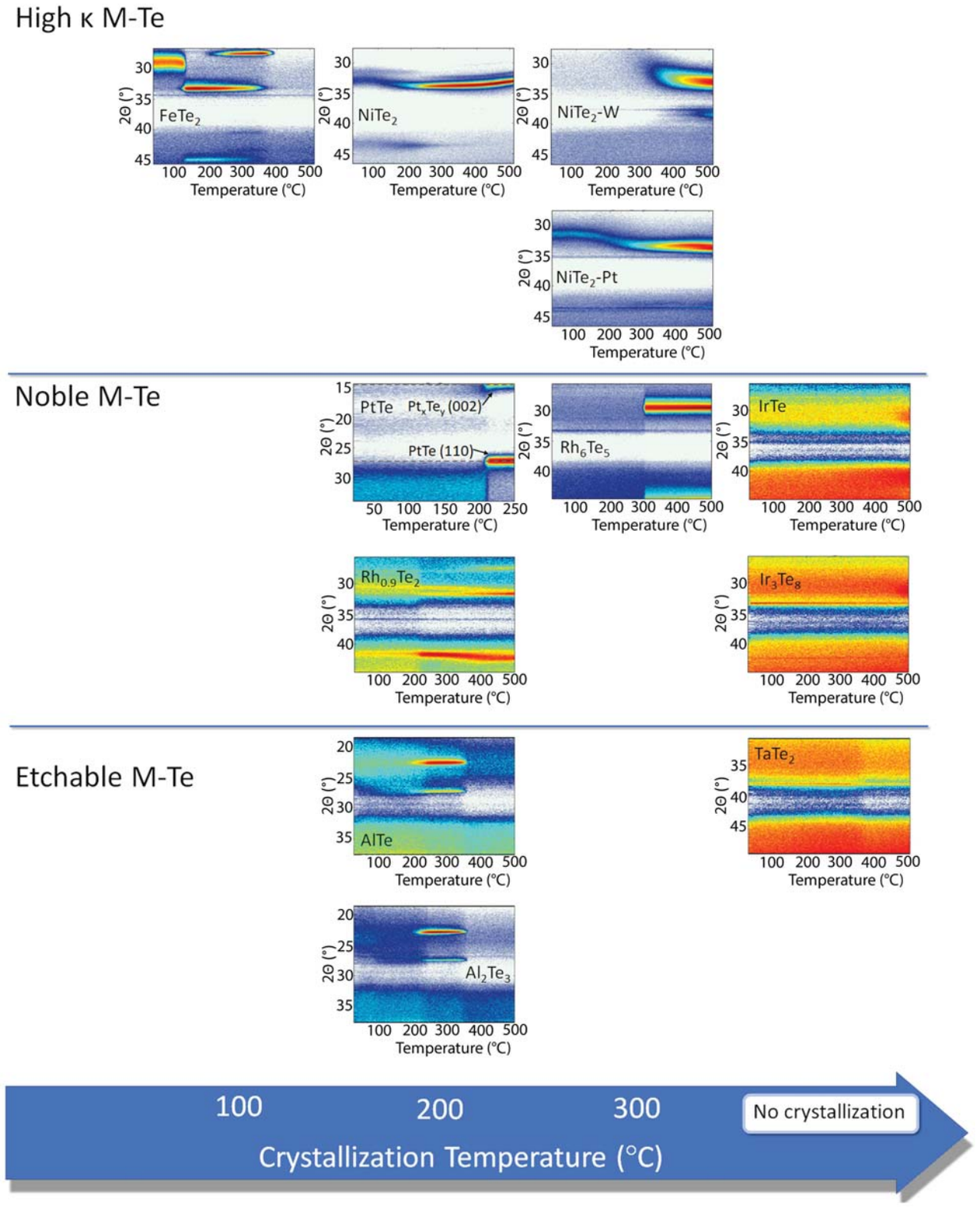

Journal of Vacuum Science Technology B

PLEASE CITE THIS ARTICLE AS DOI: 10.1116/1.5125662

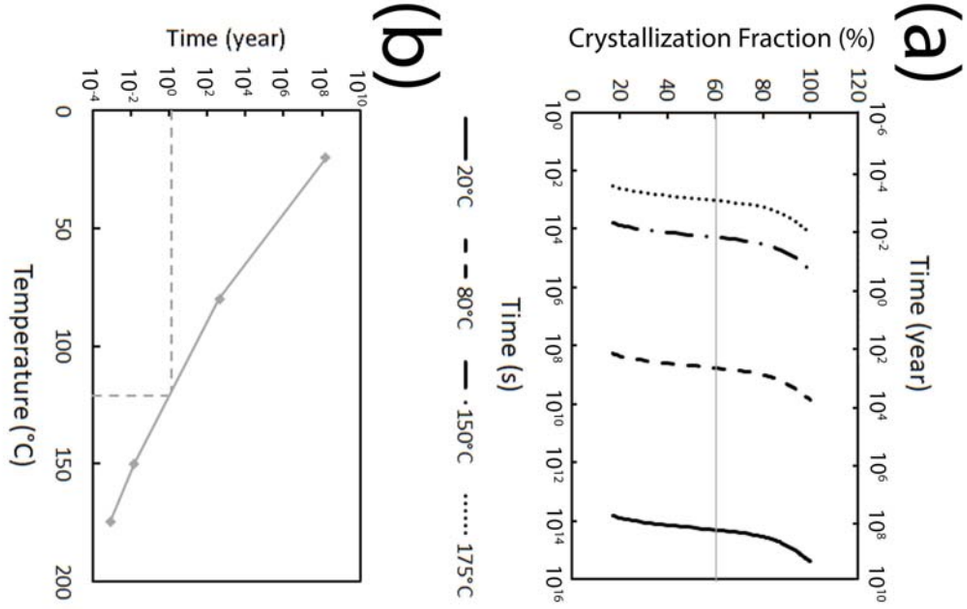

Journal of Vacuum Science Technology B

PLEASE CITE THIS ARTICLE AS DOI: 10.1116/1.5125662

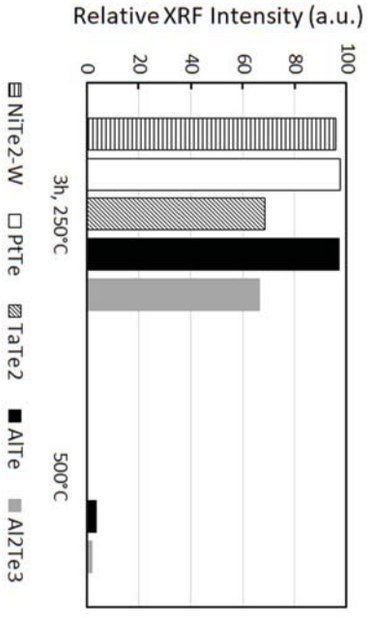

Journal of Vacuum Science Technology B

PLEASE CITE THIS ARTICLE AS DOI: 10.1116/1.5125662

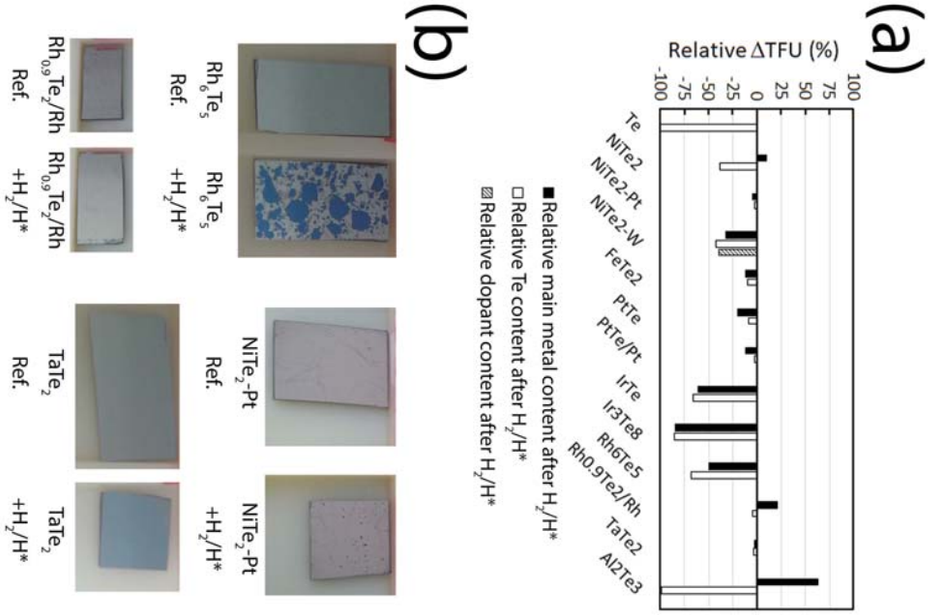

Journal of Vacuum Science Technology B

PLEASE CITE THIS ARTICLE AS DOI: 10.1116/1.5125662

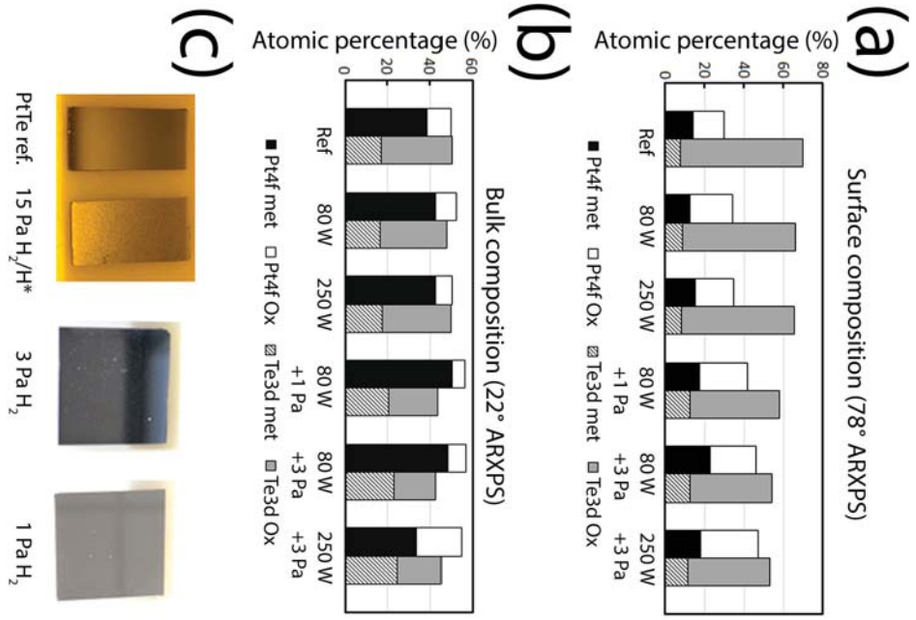

Journal of Vacuum Science Technology B

PLEASE CITE THIS ARTICLE AS DOI: 10.1116/1.5125662

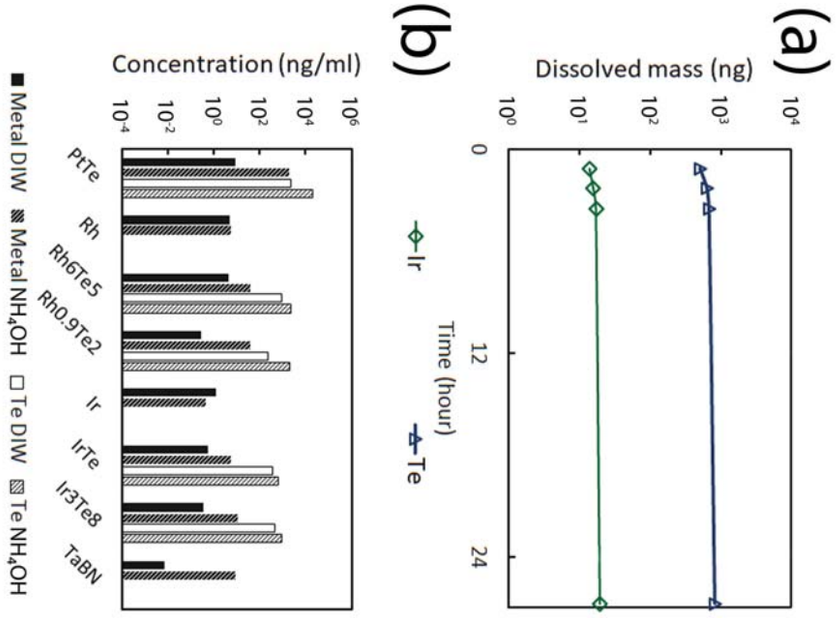

Journal of Vacuum Science Technology B

PLEASE CITE THIS ARTICLE AS DOI: 10.1116/1.5125662

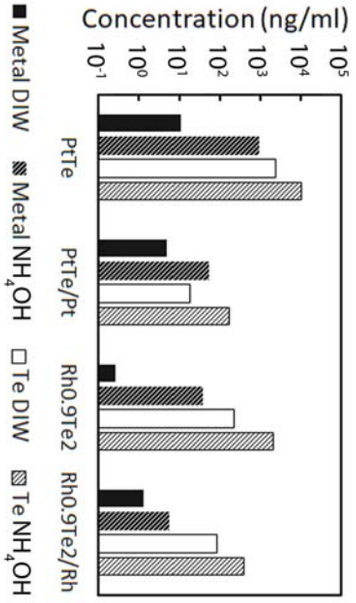

Journal of Vacuum Science Technology B

PLEASE CITE THIS ARTICLE AS DOI: 10.1116/1.5125662

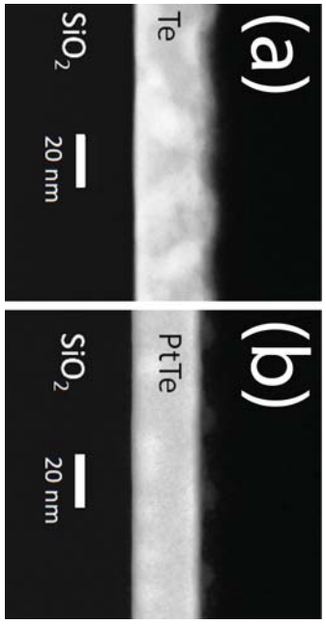

Journal of Vacuum Science Technology B

PLEASE CITE THIS ARTICLE AS DOI: 10.1116/1.5125662